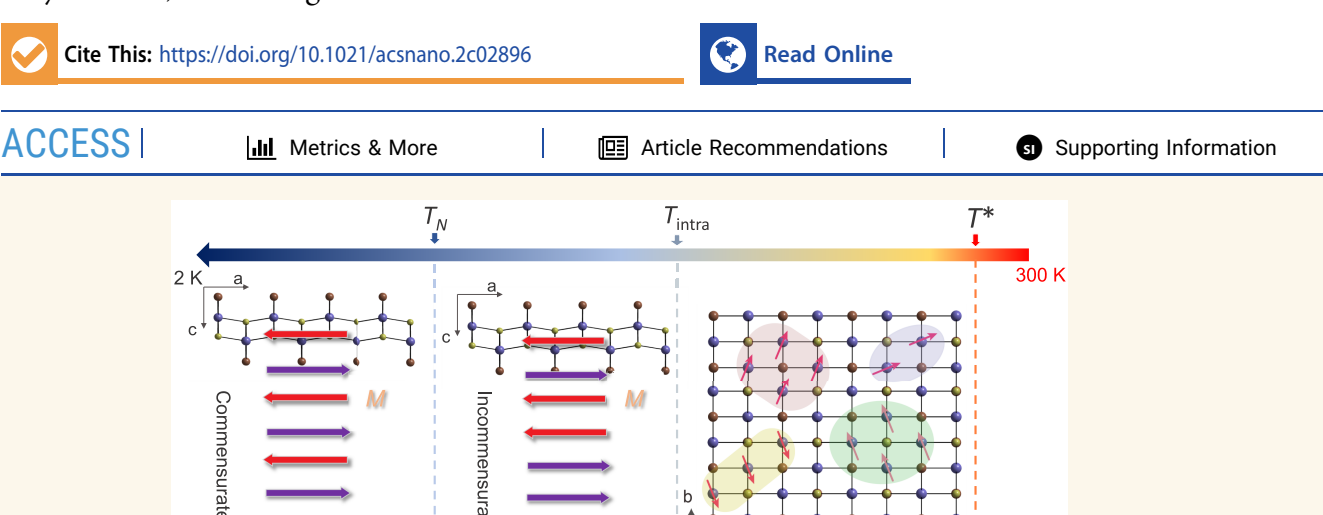


www.acsnano.org

# A Three-Stage Magnetic Phase Transition Revealed in Ultrahigh-Quality van der Waals Bulk Magnet CrSBr

Wenhao Liu,<sup>†</sup> Xiaoyu Guo,<sup>†</sup> Jonathan Schwartz, Hongchao Xie, Nikhil Uday Dhale, Suk Hyun Sung, Aswin Lakshmi Narayanan Kondusamy, Xiqu Wang, Haonan Zhao, Diana Berman, Robert Hovden,\* Liuyan Zhao,\* and Bing Lv\*



ABSTRACT: van der Waals (vdW) magnets are receiving ever-growing attention nowadays due to their significance in both fundamental research on low-dimensional magnetism and potential applications in spintronic devices. The high crystalline quality of vdW magnets is the key to maintaining intrinsic magnetic and electronic properties, especially when exfoliated down to the two-dimensional limit. Here, ultrahigh-quality air-stable vdW CrSBr crystals are synthesized using the direct solid—vapor synthesis method. The high single crystallinity and spatial homogeneity have been thoroughly evidenced at length scales from submm to atomic resolution by X-ray diffraction, second harmonic generation, and scanning transmission electron microscopy. More importantly, specific heat measurements of ultrahigh-quality CrSBr crystals show three thermodynamic anomalies at 185, 156, and 132 K, revealing a stage-by-stage development of the magnetic order upon cooling, which is also corroborated with the magnetization and transport results. Our ultrahigh-quality CrSBr can further be exfoliated down to monolayers and bilayers easily, providing the building blocks of heterostructures for spintronic and magneto-optoelectronic applications.

**KEYWORDS:** 2D magnet, vdW magnet, specific heat, second harmonic generation, scanning transmission electron microscopy, ultrahigh crystalline quality

he advance of two-dimensional (2D) van der Waals (vdW) materials with thickness down to the atomic limit has received widespread attention in the research community. The discoveries of 2D ferromagnetism with easy-axis anisotropy in vdW  $\rm Cr_2Ge_2Te_6$  and  $\rm CrI_3$  atomic layers have offered platforms for studying 2D magnetism and building blocks for integrating spintronic and magneto-optoelectronic devices. Sooner after, many other magnetic phases and tunable properties have been discovered in 2D magnets, both in their thin-film and bulk forms. For example, bulk  $\rm Fe_3GeTe_2$  (FGT) shows itinerant ferromagnetism with  $T_c = 220-230$ 

K,<sup>4,5</sup> which can be enhanced to room temperature via ionic liquid gating in the monolayer.<sup>6</sup> Cr<sub>2</sub>Ge<sub>2</sub>Te<sub>6</sub> shows a semiconducting behavior and possesses a ferromagnetic transition

Received: March 23, 2022 Accepted: September 21, 2022



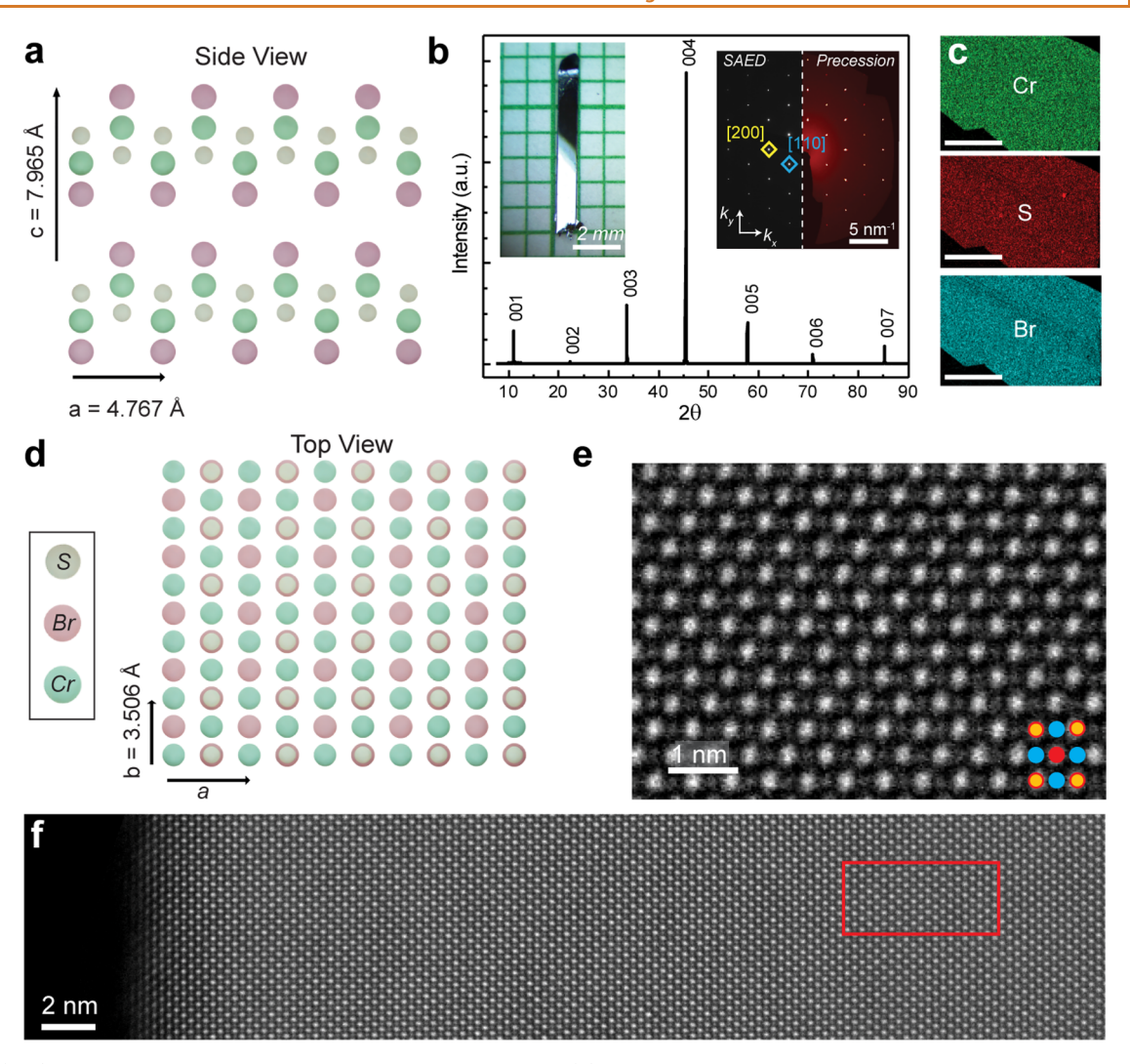


Figure 1. (a, d) Crystal structures of CrSBr viewed from b- and c-axes. (b) XRD pattern with Miller indices on CrSBr single crystals. The left inset shows the optical image of the pristine CrSBr single crystal on the millimeter grid. The right inset shows a SAED pattern along [001] and a precession image of (hk0) zone constructed by using a set of 1209 measured  $\omega$ -scan frames. (c) EDX mapping of CrSBr, suggesting uniform distributions of constitute elements throughout the crystal. Scale bar, 250  $\mu$ m. (e, f) HAADF-STEM images of the CrSBr crystal highlighting the presence of minimal defects over a 35 nm field-of-view.

temperature of 65 K in bulk, 1,7 but can be tuned to 180 K in the few-layered samples when using solid ion conductors as the gate dielectric.8 Chromium trihalides are another big family of 2D magnets. Whereas bulk CrCl<sub>3</sub> single crystals show an inplane antiferromagnetic (AFM) order below 17 K, 9,10 CrBr<sub>3</sub> shows out-of-plane ferromagnetism below  $T_c = 37 \text{ K}^{11}$  and CrI<sub>3</sub> hosts an out-of-plane ferromagnetic transition at about 61 K. 12,13 Besides, layer-dependent magnetism has been found in CrCl<sub>3</sub> and CrI<sub>3</sub>, from ferromagnetic (FM) in a monolayer to AFM in a few layers, and back to FM in bulk. 14,15 The halide atoms play an important role in determining the magnetic texture. Interestingly, as the Cr-Cr distance increases with the halogen size from Cl to Br to I, the direct exchange interaction is supposed to be weakened. This means that the superexchange mechanism, which prefers to form FM alignment, plays a more important role in the chromium trihalides series. 16 In addition, from Cl to Br to I, the spin-orbit coupling (SOC) strength increases, resulting in the evolution of spin anisotropy from the easy plane to nearly isotropic and to the easy-axis type. 17 Furthermore, by tuning the chemical ratio of halide elements, the easy axis can be tuned in

 ${\rm CrCl_{3-x}Br_{xr}}$  and frustrated magnetic regions are demonstrated in the phase diagram of  ${\rm CrCl_{3-x-y}Br_xI_y}^{18,19}$ 

The weak interlayer coupling in 2D materials/magnets allows the vertical stacking of the same or different atomic layers, where various behaviors that are not accessible in individual layers may be introduced. For instance, the magnetic proximity effect probed by the Zeeman spin Hall effect through nonlocal measurements is observed in graphene/ CrBr<sub>3</sub> heterostructures.<sup>20</sup> A large anomalous Hall effect is observed in the Cr<sub>2</sub>Ge<sub>2</sub>Te<sub>6</sub>/(Bi,Sb)<sub>2</sub>Te<sub>3</sub> heterostructure, showing that exchange coupling between the two different layers is strong and a sizable exchange gap opens in the surface state.<sup>21</sup> An antisymmetric magnetoresistance effect is observed in the Fe<sub>3</sub>GeTe<sub>2</sub>/Graphite/Fe<sub>3</sub>GeTe<sub>2</sub> trilayer heterostructures, which is proposed to result from a spin-polarized current induced by spin-momentum locking at the graphite/FGT interface.<sup>22</sup> Similar antisymmetric magnetoresistance is observed in the AFM/FM heterostructure of MnPS<sub>3</sub>/ Fe<sub>3</sub>GeTe<sub>2</sub>.<sup>23</sup> More recently, different magnetic states are discovered in moiré superlattices of twisted CrI<sub>3</sub> layers.<sup>24-26</sup> However, most of the 2D magnets have an out-of-plane easy

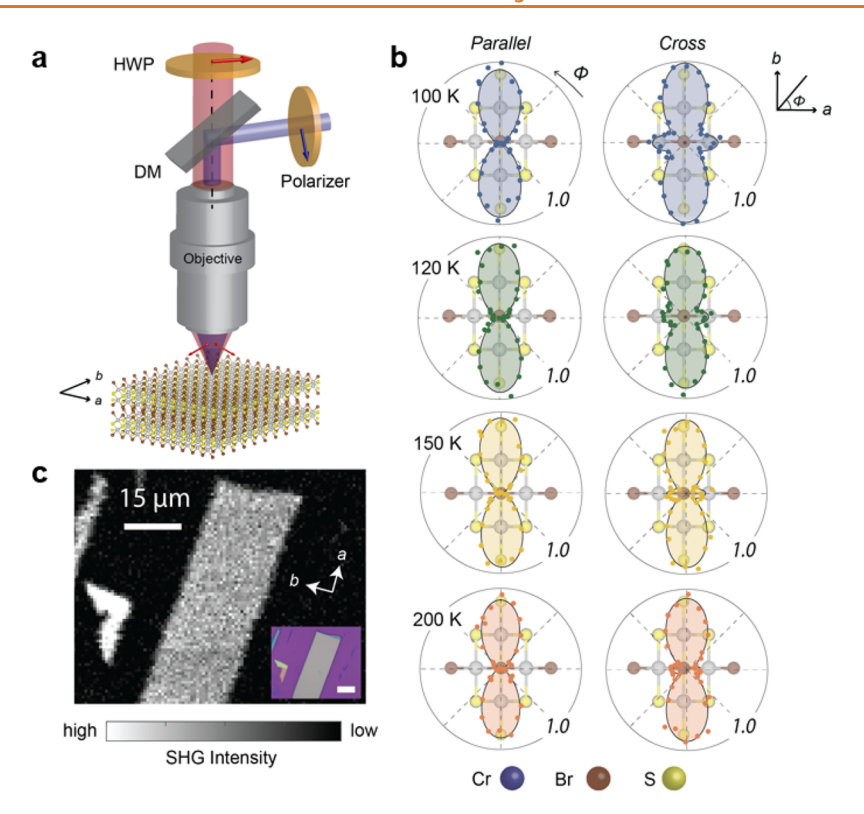


Figure 2. (a) Schematic of the SHG experimental setup. The incident fundamental and the reflected SHG light are in red and blue, respectively. Red arrows indicate the incident light polarizations while the blue arrow indicates the selected reflected SHG light polarization. HWP: half wave plate, DM: dichroic mirror. (b) Polar plots of SHG RA in both the parallel and the crossed channels at selected temperatures. The experiment data (filled circles) are well fitted by the model based on group theory analysis (solid lines). All plots are of the same intensity scale, normalized to a value of 1.0 corresponding to 35 pW. The CrSBr crystal structures are overlaid in the background. Inset shows the definition of polar angle  $\phi$  that is the angle between the incident light polarization and the crystal axis a. (c) Scanning SHG image of the bulk CrSBr sample measured at  $\phi = 90^{\circ}$  in the parallel channel at 80 K. Inset shows the corresponding wide-field optical image. The scale bar of the inset is 15  $\mu$ m.

axis, which are severely affected by the vertical heterostructure integration. Moreover, many of the 2D magnets are limited to their low magnetic transition temperature, and the research of atomic thin vdW magnets is often hindered by their extreme sensitivity to air and degraded properties during the fabrication process. Thus, the pursuit of 2D magnetic materials with preferably an in-plane magnetic easy axis, better crystal and exfoliation qualities, higher air stability, and better interfacial properties will be rather rewarding in the 2D magnets studies.

Very recently, an air-stable 2D AFM CrSBr with a high Néel temperature  $T_N = 132$  K has been reported. As shown in Figure 1a,d, the Cr-S framework is sandwiched by Br atoms, forming one layer of CrSBr. Both Cr and S are octahedrally coordinated, and each layer of CrSBr is weakly coupled via the vdW force along c direction, resulting in the easy exfoliation of this material. Besides the high magnetic transition temperature, the single layer of CrSBr shows a FM order, and these FM layers couple antiferromagnetically along the c-axis. The monolayer is also demonstrated to be air-stable and shows an in-plane FM order below 146 K based on second harmonic generation (SHG) results.<sup>29</sup> Furthermore, a strong spin-charge coupling is observed in the graphene/CrSBr heterostructure, which is due to a large induced exchange interaction by the proximity of the AFM CrSBr. 30 To further facilitate the future heterostructure and device studies of this material, high-quality bulk crystals which enable a better and large-area exfoliation will be necessary.

Currently, CrSBr is usually synthesized through the chemical vapor transport (CVT) method using chromium metal and S<sub>2</sub>Br<sub>2</sub> sealed in quartz ampule in two-zone tube furnaces.<sup>27,2</sup> However, vdW materials grown from the CVT method often present more defects than other methods, 31,32 which potentially impacts the magnetic order in 2D. Besides, S<sub>2</sub>Br<sub>2</sub> here plays a joint role of transport agent and reactants, which would cause the crystal to cluster together easily and hinder the size and quality of the single crystal. Herein, we present a simpler and more direct solid-vapor synthesis method, which yields much bigger size and higher quality of crystals than the conventional CVT method. The high single crystallinity and homogeneity of the single crystals have been thoroughly evidenced at different length scales by X-ray diffraction (XRD), second harmonic generation rotational anisotropy (SHG RA), and scanning transmission electron microscopy (STEM), respectively. More importantly, the specific heat measurements of our sample reveal a three-stage development of the magnetic order upon cooling, which is corroborated with the magnetization and transport results.

# **RESULTS AND DISCUSSION**

Figure 1b shows the optical images and the XRD pattern of the CrSBr single crystal. The black and shiny single crystals with a lateral size as large as 7 mm  $\times$  1 mm are typically obtained (more optical images in Supplemental Figure S1). Only 00*l* peaks can be observed as expected, since the flat surface is perpendicular to the crystallographic *c*-axis. The full-width at

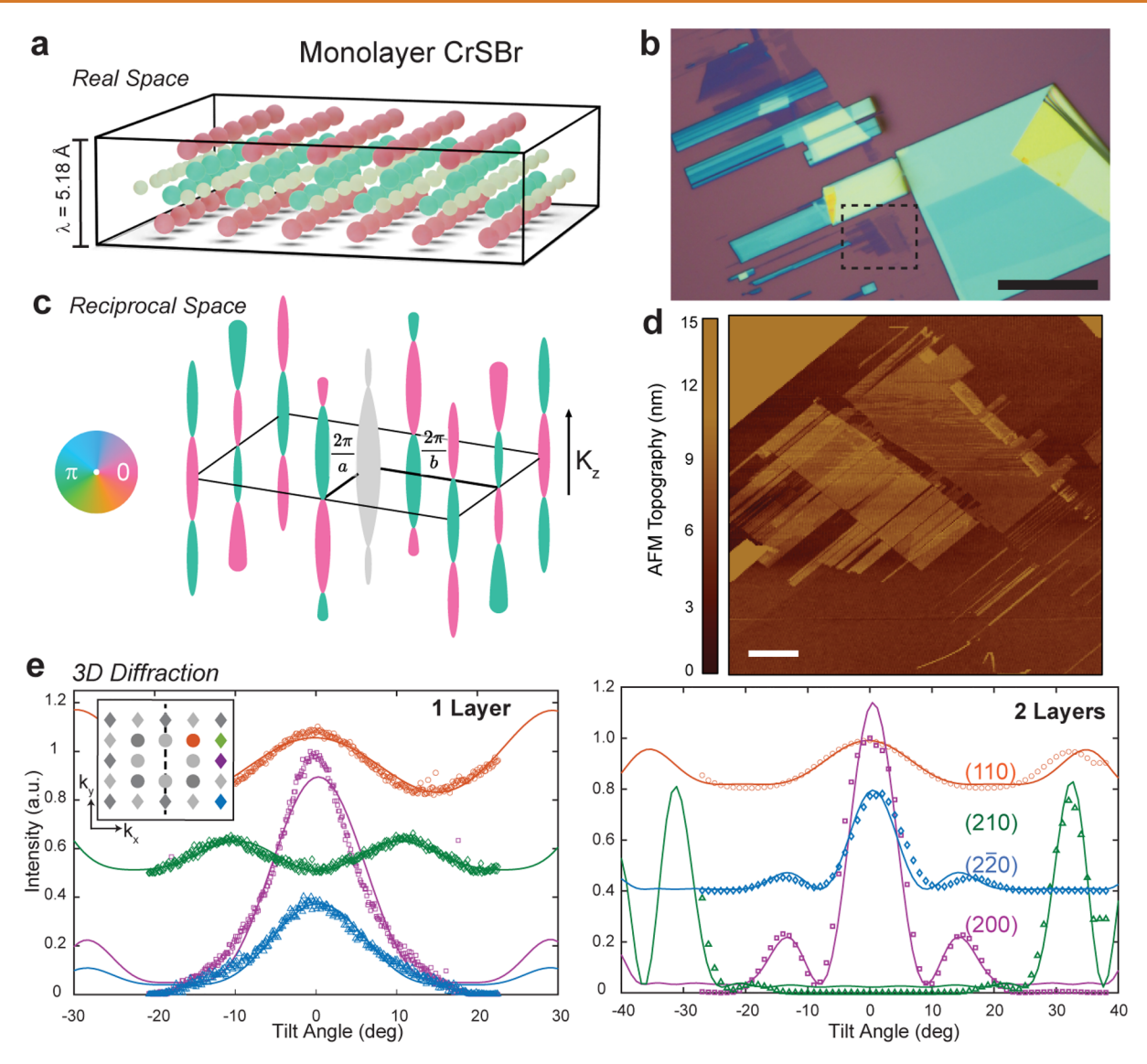


Figure 3. (a) Schematic illustration of monolayer CrSBr. (b) Optical image of thin CrSBr flakes deposited onto a  $SiO_2/Si$  wafer substrate via mechanical exfoliation. (c) Schematic of calculated out-of-plane momentum  $(k_z)$  dependence for various Bragg rods of monolayer CrSBr. The thickness and color indicate the complex magnitude and phase of the structure factor, respectively. (d) Atomic force microscopy topography of exfoliated CrSBr flakes. (e) Experimental Bragg intensities (scatter points) for (110) (orange), (220) (blue), (200) (purple), and (210) (green) peaks plotted as a function of tilt angle, which strongly agree with the fitted kinematic models.

half-maximum of the peaks is as narrow as 0.04°, which indicates the large crystalline domains and no noticeable inhomogeneous strain fields within samples. Procession X-ray and electron diffraction (Figure 1b, inset) clearly demonstrate the single-crystal nature with sharp Bragg peaks without distortions such as ring shapes or blurry spots, suggesting nearperfect single crystallinity without noticeable grain boundaries or distortions in the samples over a  $\sim$ 100  $\mu$ m length scale. This is also reflected by the refinement results ( $R_1$ = 1.35% and  $wR_2$ = 3.51%, refinement details shown in Supplemental Table S1). Furthermore, we construct procession images along the three (0kl), (h0l), (hk0) plane directions pixel-by-pixel from the complete sets of single-crystal XRD ω-scan images (1209 frames). As the precession images have detailed information on diffraction layers in the reciprocal space, it provides a direct and clear viewpoint on the crystal quality. The three procession images, shown in the inset of Figure 1b and Supplemental Figure S2, further demonstrate no noticeable crystal twining or

lattice distortion in three dimensions in our single-crystal samples. The lattice parameters of CrSBr at 170 and 296 K are shown in Supplemental Table S1. The energy dispersive X-ray (EDX) spectroscopy mapping (Figure 1c) suggests uniform distributions of constitute elements throughout the crystal. Moreover, the EDX spectra yields the Cr:S:Br molar ratio as 33.36(21)%:33.02(22)%:33.12(19)%, which is very close to the stoichiometric ratio of 1:1:1.

We further demonstrate the high crystalline quality of CrSBr at the atomic scale in mechanical exfoliated atomic layers. Atomically resolved high-angle annular dark-field (HAADF)-STEM measurements (Figure 1e,f and Supplemental Figure S3) confirm the absence of atomic defects, grain boundaries, or changes in the stacking order in thin CrSBr flakes. The HAADF-STEM images show Cr and S-Br atomic columns viewed in projection as a cubic pattern with alternating dim (Cr) and bright spots (S-Br). The crystal uniformity is observed to the edge of the specimen (Figure 1f).

Furthermore, the selective area diffraction pattern (SAED) (Figure 1b inset) reveals sharp Bragg spots with an in-plane two-fold symmetry, which agrees with the lattice periodicity of CrSBr.

Second, to further characterize the homogeneity of the single crystal in the micron length scale, we have carried out SHG RA measurements on bulk CrSBr under the nominal normal incidence geometry. Figure 2a shows the schematic of the experimental setup. A long working distance 20× objective with a 0.4 numerical aperture (NA) focuses the 800 nm incident laser beam onto the sample surface. The relatively large NA yields a cone-shaped focused beam, covering the incident electric field polarizations from perfectly parallel to the sample surface to 23.5°, i.e., arcsin(NA), off from it. A dichroic mirror (DM) set, together with a bandpass filter set, selects the 400 nm SHG light and directs it to a photomultiplier-tube detector that is connected to a current amplifier and then a lock-in amplifier. The polarizations of the incident and the reflected light can be selectively chosen using a halfwave plate (HWP) and a polarizer, respectively.

We have performed SHG RA measurements to verify the structural symmetries at various temperatures across the AFM phase transition temperature  $T_N = 132$  K. Figure 2b shows the polar plots of SHG intensity as a function of the incident polarization angle  $\phi$  away from the a-axis (Figure 2b inset) in two channels where the incident fundamental and the reflected SH light polarizations are parallel (parallel) and perpendicular (cross) to each other. We clearly see that all RA patterns show two mirrors normal to crystal axes a and b, consistent with the point group mmm determined by our XRD measurement (space group Pmmn, no. 59, see Supplemental Table S1). Furthermore, we observe that from 100 to 200 K, the SHG RA results in the parallel channel remains nearly constant including both the shape and the amplitude, whereas those in the crossed channel shows a modest evolution. The two smaller lobes in SHG RA patterns of the crossed channel along the a-axis gradually shrink as the temperature increases, while the two larger lobes along the *b*-axis barely change in intensity. The absence of significant changes in both channels across  $T_{\rm N}$ = 132 K is consistent with the same mmm point group for both the paramagnetic phase above  $T_N$  and the layered AFM phase below  $T_N$ , demonstrating the robust and consistent crystal structure of the samples. Usually, the two-fold rotation symmetry operation along the c-axis should forbid any SHG radiation in the normal incidence geometry, including both the electric dipole and the electric quadrupole contributions. Our observed nonzero SHG RA signal is attributed to the electric quadrupolar contribution from the large NA-induced oblique light rays (Figure 2a). We further simulated the SHG RA functional form by computing the electric quadrupolar SHG under the mmm point group and then taking an average over the full azimuthal direction at an oblique angle  $\theta = \arcsin(NA)$ [see Supporting Information]. The experimental data are well fitted by this model as shown in Figure 2b.

In addition to the single-spot SHG RA measurement to confirm the point symmetry, we have also performed scanning SHG microscopy measurements to examine the spatial homogeneity at a spatial resolution of sub $\mu$ m and a length scale of several tens of  $\mu$ m. Figure 2c shows an SHG scanning image measured at  $\phi = 90^{\circ}$  in the parallel channel at 80 K, showing a uniform distribution of the SHG intensity, further confirming the structural and magnetic homogeneity of the sample at the micron scale.

Monolayer (Figure 3a) and bilayer are readily fabricated as large, single crystals from the bulk using mechanical exfoliation, as confirmed with AFM and 3D reciprocal space measurements.<sup>33</sup> Figure 3d shows an AFM image of monolayer and bilayer CrSBr flakes indicated by the black dash square of the wide-field optical microscopy image shown in Figure 3b, which can be routinely obtained by mechanical exfoliation from bulk single crystals. By tilting the sample, we can measure the diffraction spots as a function of out-of-plane crystal momentum (k<sub>z</sub>). A schematic of the 3D Bragg structure for several monolayer CrSBr peaks are shown in Figure 3c. The experimental Bragg rod intensities are shown in Figure 3e as discrete points together with their expected values in solid lines. As the k<sub>z</sub> dependence for bilayer flakes is noticeably different from that for monolayers, we can confirm our ability to exfoliate CrSBr crystals down to monolayer thickness. In addition, fitting the k<sub>z</sub> dependence for the Bragg peaks provides direct quantification for the out-of-plane spacing between two adjacent elements. Specifically, we experimentally measured  $\Delta Cr = 0.90 \pm 0.16$  Å,  $\Delta S = 0.61 \pm 0.09$  Å,  $\Delta Br =$  $2.59 \pm 0.19$  Å and  $c = 7.91 \pm 0.288$  Å for the bilayer CrSBr crystal. These bilayer CrSBr preserves its structure after several months of intermittent air exposure, further demonstrating the air stability of these thin CrSBr thin flakes (Supplemental Figure S4). Moreover, our thermal stability data also show that the thin flakes maintain their symmetry and structure across room temperature to 523 K upon heating (Supplemental Figure S5)

Given the high crystalline quality of these CrSBr crystals, we revisit the thermodynamic properties of bulk CrSBr. First, low-temperature (below 25 K) specific heat behaviors of CrSBr without external magnetic fields are shown in the inset of Figure 4, which can be fitted using the Debye model  $C_p = \gamma_n T$ 

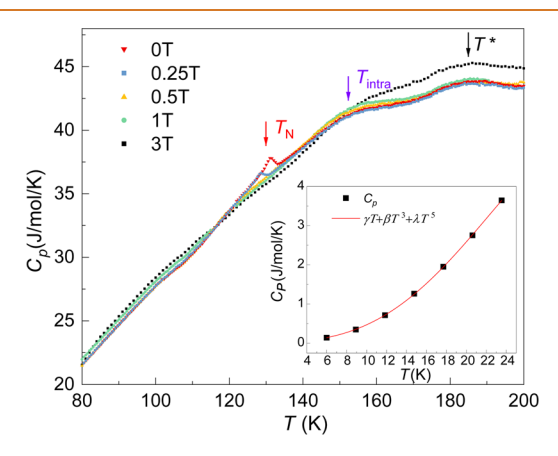


Figure 4. Specific heat  $C_p(T)$  at temperatures from 80 to 200 K under various external magnetic fields applied along the c direction of the CrSBr single crystal. Three specific anomalies are marked as  $T_{\rm N}$ ,  $T_{\rm intra}$ , and  $T^*$ , respectively. The inset shows the fitting of the specific heat from 6 to 24 K using the Debye model  $C_p = \gamma T + \beta T^3 + \eta T^5$ .

+  $\beta T^3$  +  $\eta T^5$ , where  $\gamma_n T$  and  $\beta T$  <sup>3</sup> +  $\eta T^5$  are from the electron and phonon contributions, respectively. The parameters obtained from the fitting results are  $\gamma_n = 9.8$  mJ/mol/K<sup>2</sup>,  $\beta = 0.396$  mJ/mol/K<sup>4</sup>, and  $\eta = -2.4 \times 10^{-4}$  mJ/mol/K<sup>6</sup>. The Debye temperature  $\Theta_D$  thus can be estimated using the

relation 
$$\Theta_D = \left(\frac{12\pi^4 k_{\rm B} N_{\rm A} Z}{5\beta}\right)^{1/3}$$
 to be  $\Theta_D = 245$  K, where  $N_{\rm A}$  is

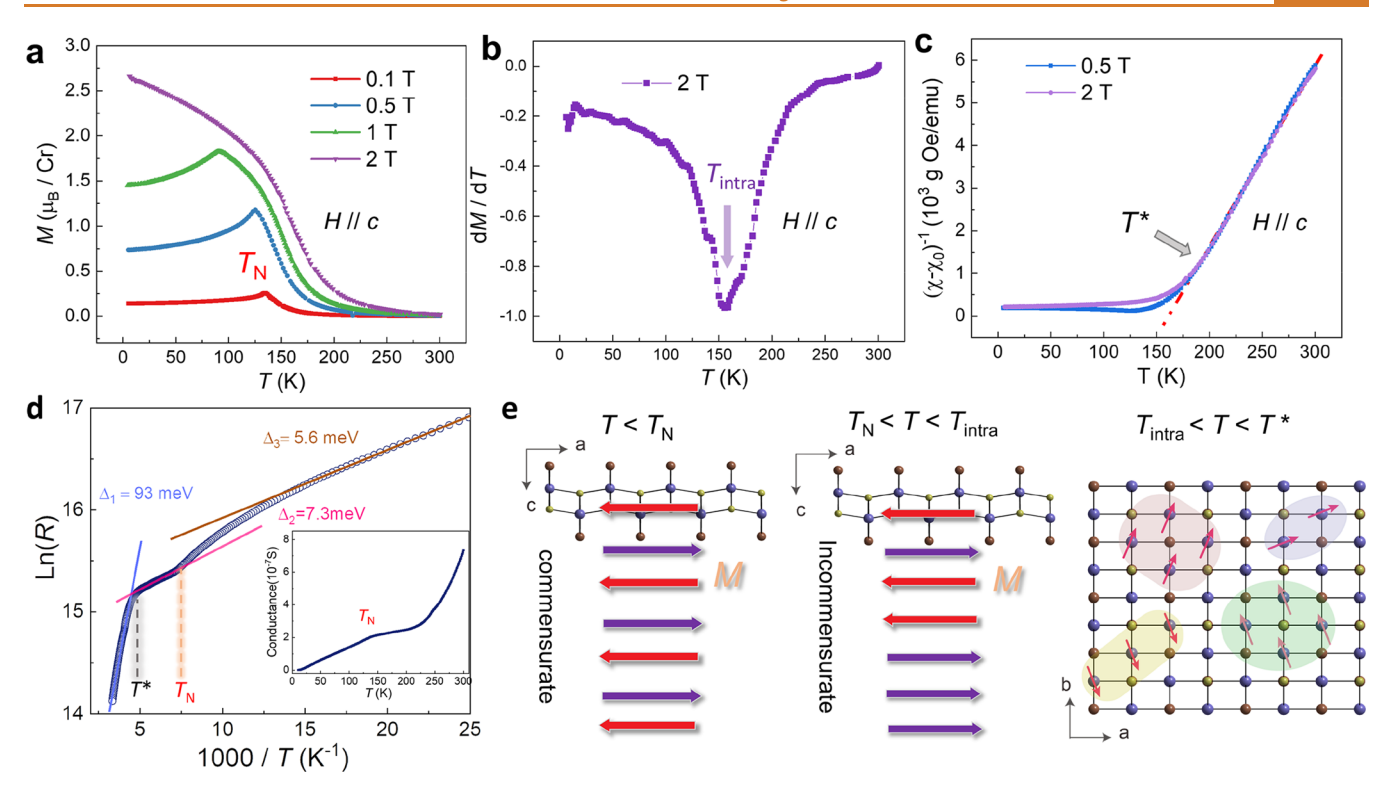


Figure 5. Magnetization and transport behaviors of CrSBr. (a) Temperature-dependent magnetization with various magnetic fields applied parallel to c-axis. (b) dM/dT curve of the magnetization under the external magnetic field of 2 T, where the AFM order is completely suppressed, indicating a phase transition at 155 K. (c) Temperature dependence of the inverse magnetic susceptibility with magnetic fields of 0.5 and 2 T applied parallel to the c-axis. The red line shows the fitting of our data using the Curie—Weiss law, where a deviation occurs around 185 K. (d) Ln(R) vs 1/T. Transport behaviors of bulk CrSBr single crystal are fitted using the thermal activation model. The gap changes across the specific heat anomaly temperatures. Inset: temperature dependence of in-plane conductivity of CrSBr. (e) Schematic magnetic structures of CrSBr upon cooling. The red and purple arrows in the first two panels indicate the directions of magnetic moments in CrSBr layers and M stands for magnetization. The color-shaded ellipses here highlight the local magnetic orders developed.

the Avogadro constant and Z is the number of atoms in one unit cell. The nonzero  $\gamma_n$  in the semiconducting phase here may be associated with a constant density of states of AFM excitations near the Fermi surface, which are discovered in many 2D semiconducting magnets.<sup>34</sup>

Second, in the high-temperature region (80-200 K) with applied magnetic fields parallel to the c-axis of the CrSBr single crystals shown in Figure 4, three distinct specific heat anomalies can be observed. From low to high temperatures, the first clear sharp peak is at 132 K without applied magnetic fields. Upon increasing the magnetic field, this peak gets suppressed toward lower temperatures until disappearing above 0.5 T, which is a typical behavior of AFM phase transitions happening at the Néel temperature  $T_N$ . The second hump occurs at ~155 K with a clear change of the slope. This transition temperature gets enhanced by applying magnetic fields, which is reminiscent of the intralayer FM coherence (or order). The third anomaly with its temperature denoted as  $T^*$ , which has not been observed previously, occurs around 185 K and remains nearly unchanged under external magnetic fields up to 3 T. The heat capacity measurement of CrSBr with external magnetic fields applied along the b-axis (easy axis) has also been carried out (Supplemental Figure S6). The behaviors of the heat capacity as a function of temperature measured with the external magnetic fields aligned with the crystal c- and b-axes do not show significant differences, and all the three magnetic transitions can be observed. This transition at  $T^*$ with B // b-axis shown in  $C_p$  (Figure S6a) gets blurred

compared to that with B // c-axis (Figure 4), which is due to the relatively weaker coupling coefficient near  $T^*$  ( $\sim$ 80%) between the vertically aligned sample slabs and the heat capacity platform.

It comes to our attention that in the isostructural compound CrOCl, similar three specific heat anomalies have also been observed in the high-quality crystals. CrOCl shows an AFM order below  $T_{\rm N}=13.5$  K. At 26.7 and 27.8K, two other anomalies emerge, which are related to the formation of incommensurate magnetic superstructure and a structural phase transition. However, for our crystals, single-crystal XRD at 170 K (Supplemental Table S1) and SHG RA measurements (Figure 2) down to 100 K do not show any symmetry change nor structural transition in the bulk crystals.

To investigate further these thermodynamic anomalies, magnetization together with transport measurements have been carried out. Figure 5a exhibits the temperature dependence of magnetizations for bulk CrSBr single crystals in the magnetic fields ranging from 0.1 to 2 T applied along c-axis. A peak around 132 K under 0.1 T stands out clearly. Upon increasing the external magnetic field, this peak becomes broader and shifts to lower temperatures and disappears above 2 T, which is a classic behavior for AFM phase transitions consistent with the specific heat anomaly at  $T_{\rm N}$ . Besides, the temperature dependence of magnetizations with fields applied along a-axis is shown in Figure S7, where the AFM order is totally suppressed above 1 T. The magnitudes of the magnetic field that suppress the AFM order along a- and c-axes are very

different, demonstrating strong magnetic anisotropy in CrSBr. In addition, near the low-temperature limit of 2 K in Figure 5a, magnetization measured along the c-axis reaches a value of 2.75  $\mu_{\rm B}/{\rm Cr}$  under 2 T, which is very close to the expected value of 3  $\mu_{\rm B}$  expected for the trivalent Cr with an electronic configuration 3d³, indicating nearly all the moments are ferromagnetically aligned along the c-axis. It is worthwhile noting that in a recent report, Telford et al. observed a magnetization hump around 40 K in their CrSBr sample, which is attributed to a hidden low-temperature magnetic order related to magnetic defects.³ However, such a magnetization hump is absent from the magnetization measurements on our high-quality samples.

Figure 5b plots the temperature dependence of dM/dT under the magnetic field of 2 T along the c-axis when the longrange AFM order is completely suppressed. A clear dip, indicating a phase transition near 155 K, can be clearly seen and is consistent with the specific heat anomaly occurred at  $T_{\rm intra}$ . This phase transition is attributed as the occurrence of the intralayer superexchange coupling and an intermediate ferromagnetic phase (iFM), where the FM order within the plane is established, while the interlayers show an incommensurate magnetic order.

The inverse magnetic susceptibilities under 0.5 and 2 T are shown in Figure 5c and demonstrate the deviations from the Curie—Weiss behavior at ~185 K. The red line in Figure 5c is the fitting result by using inverse magnetic susceptibilities through the modified Curie—Weiss law:

$$\chi = \chi_0 + \frac{C}{T - T_0}$$

where  $\chi_0$  is the temperature-independent susceptibility arising from the background, C is the Curie–Weiss constant, and  $T_0$  is the Curie temperature. The yielding values are  $\chi_0 = -1.4 \times 10^{-4}$  emu/g/Oe, C = 0.0226 emu K/g/Oe, and  $T_0 = 164$  K for the magnetization under 0.5 T and  $\chi_0 = -1.4 \times 10^{-4}$  emu/g/Oe, C = 0.0231 emu K/g/Oe, and  $T_0 = 163$  K for the magnetization under 2 T.

The temperature of the deviation from the Curie—Weiss behavior is close to  $T^*$ , the third anomaly in the specific heat results. Previously we have demonstrated no structure or crystal symmetry changes across  $T^*$ . Instead, this broad hump at  $T^*$  in the specific heat could be related to the emergence of the spin—spin correlations. Upon increasing the magnetic field to 3 T, the broad hump keeps nearly the same both in the temperature and the magnitude, which is reminiscent of that found in frustrated magnetic systems. A plausible scenario here is that the short-range magnetic order begins to establish within each CrSBr layer, while the long magnetic order within the layer is still prohibited due to strong thermal fluctuations. Only when the temperature decreases to  $T_{\rm intra}$  can the long-range magnetic order in each layer develop.

Those specific heat anomalies are also reflected in the transport results. The inset of Figure 5d shows the temperature dependence of the conductance of bulk CrSBr. A clear change of the conductance slope can be observed around 132 K, which is attributed to the AFM phase transition. Figure 5d shows Ln(R) vs (1000/T). Three linear relations, which are consistent with the standard thermal activation model, <sup>40</sup> can be observed in different temperature regimes. The gap above  $T^*$  is estimated to be about 93 meV and decreases dramatically to 7.3 meV for  $T_N < T < T^*$ . Such a drastic change of the gap reflects the strong coupling between the magnetic order and

the transport behaviors in this material. The gap gets modified further for  $T < T_{\rm N}$  and finally decreases to 5.6 meV until 10 K. It is noted that  $T_{\rm intra}$  is not reflected in the transport results, which may be because the incommensurate magnetic order is established among adjacent layers at  $T_{\rm intra}$ , while the temperature dependence of resistance here is measured within the layer of the CrSBr single crystal. Instead, the out-of-plane resistance measurement may reveal distinct features at  $T_{\rm intra}$ , which needs future investigation.

The specific heat anomalies together with the magnetization and transport results indicate that the magnetic order gradually develops in three different stages upon cooling, as is illustrated in Figure 5e: (1) From room temperature to  $T^*$ , the crystal shows paramagnetic orders with random spin orientations. (2) For  $T_{\text{intra}} < T < T^*$ , local or short-range magnetic order begins to establish due to the spin-spin coupling within each CrSBr layer, while the long-range magnetic order within the layer is still suppressed due to thermal fluctuations. When the temperature decreases to  $T_{\text{intra}}$  where the thermal fluctuations are reduced, the long-range magnetic order in each layer is established. (3) For  $T_N < T < T_{intra}$ , an iFM phase began to establish where the FM order within the plane is established, while the interlayers show incommensurate magnetic orders. (4) For  $T < T_N$ , a FM order within the plane together with AFM order among adjacent planes is formed.

## **CONCLUSIONS**

In conclusion, ultrahigh-quality air-stable and large-size bulk CrSBr single crystals have been synthesized directly using the solid—vapor growth method. The high single crystallinity and homogeneity of the single crystals have been thoroughly evidenced at different length scales by XRD, SHG RA, and STEM, respectively. More importantly, specific heat measurements of these ultrahigh quality CrSBr crystals show three thermodynamic anomalies at 185, 156, and 132 K, revealing a stage-by-stage development of the magnetic order upon cooling, which is also corroborated with the magnetization and transport results. Our ultrahigh-quality CrSBr can further be exfoliated down to monolayers and bilayers easily, providing the building blocks of heterostructures for spintronic and magneto-optoelectronic applications.

# **METHODS**

Sample Preparation. The CrSBr single crystal was naturally grown using the direct solid-vapor method through a box furnace. Cr powder (Alfa Aesar, 99.97%) and S powder (Alfa Aesar, 99.5%) were weighted inside the Ar-glovebox with the total oxygen and the moisture level less than 1 ppm. For the sake of easy loading of bromide, the bromide liquid (99.8%) first was solidified with the assistance of liquid nitrogen. Cr powders, S powders, and solid Br<sub>2</sub> were loaded inside the clean quartz ampule with the mole ratio of 1:1.1:1.2, which were subsequently sealed under vacuum using the liquid nitrogen trap. We found the extra amount of the S and Br creating positive vapor pressure can reduce the defects in the grown crystals. Furthermore, the slightly extra amount of Br in the reactants was proven to be effective for growing large and high-quality single crystals. The quartz ampule was heated up to 930 °C very slowly, kept at this temperature for 20 h, followed by slow cooling down to 750 °C  $(1^{\circ}/h)$ . The assemble was then quenched down to room temperature. Large CrSBr single crystals grew naturally at the bottom of the ampule. A tiny amount of CrBr3 was also found at the top of the quartz ampule and could be easily separated from the CrSBr crystals.

**X-ray Diffraction.** The powder XRD was carried out on the single crystal at room temperature using a Rigaku Smart Lab X-ray diffractometer equipped with  $Cu-K\alpha$  radiation. The single-crystal

X-ray data were measured on a Bruker SMAER diffractometer with an Apen II area detector with a Mo K $\alpha$  source ( $\lambda = 0.71073$  Å), and the collected data set was integrated using the Bruker Apex-II program, with the intensities corrected for the Lorentz factor, polarization, air absorption, and absorption due to variation in the path length through the detector faceplate. The data were scaled, and absorption correction was applied using SADABS. The structure was solved by using the intrinsic phasing method in SHELXT and refined using SHELXL with all atoms refined anisotropically. The EDX spectra were obtained using a Zeiss LEO 1530 with a beam energy of 20 kV.

Electron Microscopy. Atomically resolved HAADF-STEM images were collected using a Cs aberration-corrected JEOL 3100R05 microscope (300 keV, 22 mrad) with a camera length of 12 cm. SAED measurements were obtained on a Thermo Fisher Talos operated at 200 keV, equipped with a Gatan OneView camera.

**3D Electron Diffraction Measurements.** Acquiring 3D electron diffraction patterns was accomplished by tilting the specimen over a range of angles relative to the incident beam to provide slices through the reciprocal structure. SAED patterns were acquired on the TFS Talos operated at a voltage of 80 keV at a tilt range of ±40° with a  $0.1^{\circ}$  tilt increment for the monolayer sample and  $\pm 30^{\circ}$  with a  $1^{\circ}$  tilt increment for the bilayer. Each SAED in the tilt series is first background subtracted and aligned to a common center. Diffraction spots at every specimen tilt were characterized by fitting a fourparameter 2D Gaussian to a windowed region about each peak. The integrated diffraction peak intensity was then calculated and plotted against k, for curve fitting with the kinematic model.

Magnetization, Resistivity, and Specific Heat Measurements. DC magnetization was conducted with a Quantum Design magnetic property measurement system down to 5 K. Resistivity of bulk CrSBr single crystal with a thickness of about 0.5 mm was measured with a two-probe method using the Quantum Design physical property measurement system (PPMS) coupled with Keithley 6517b. The temperature ranged from 10 to 300 K. Specific heat measurement was done in the PPMS Dynacool by a time relaxation method with a magnetic field parallel to the crystallographic c-axis.

SHG Measurements. The incident ultrafast light source was of 50 fs pulse duration and 200 kHz repetition rate. It was focused down to a 3  $\mu$ m diameter spot on the sample normally with a power of 175  $\mu$ W. For the SHG RA measurements, the polarizations of the incident and reflected light can be selected to be either parallel or perpendicular to each other, whose azimuthal angle  $\phi$  can change correspondingly. The intensity of the reflected SHG signal was detected by a photomultiplier-tube and then amplified by an electronic current preamplifier and a lock-in amplifier in sequence. For the scanning SHG measurement, the same power and the beam size were used. A two-axis Galvo scanning mirror paired with a confocal imaging system was used to illuminate the sample at normal incidence with a constant fluence during scanning.

#### ASSOCIATED CONTENT

# Supporting Information

The Supporting Information is available free of charge at https://pubs.acs.org/doi/10.1021/acsnano.2c02896.

> Additional experimental details including additional optical image of as-grown CrSBr single crystals, precession images of two other directions, single-crystal diffraction results, STEM image over a large field of view (~65 nm), air stability of CrSBr flakes, thermal stability of CrSBr flakes, thermodynamic behavior of CrSBr with in-plane magnetic fields, magnetization with external magnetic fields applied along a-axis, and the group theory analysis on SHG RA (PDF)

#### **AUTHOR INFORMATION**

# **Corresponding Authors**

Robert Hovden – Department of Material Science and Engineering and Applied Physics Program, University of Michigan, Ann Arbor, Michigan 48109, United States; orcid.org/0000-0002-3403-8803; Email: hovden@ umich.edu

Liuyan Zhao – Department of Physics, University of Michigan, Ann Arbor, Michigan 48109, United States; oorcid.org/ 0000-0001-9512-3537; Email: lyzhao@umich.edu

Bing Lv – Department of Physics, The University of Texas at Dallas, Richardson, Texas 75080, United States; Department of Materials Science and Engineering, The University of Texas at Dallas, Richardson, Texas 75080, United States; orcid.org/0000-0002-9491-5177; Email: blv@ utdallas.edu

### **Authors**

**Wenhao Liu** – Department of Physics, The University of Texas at Dallas, Richardson, Texas 75080, United States; orcid.org/0000-0001-9757-1077

Xiaoyu Guo – Department of Physics, University of Michigan, Ann Arbor, Michigan 48109, United States; oorcid.org/ 0000-0003-2088-6112

Jonathan Schwartz - Department of Material Science and Engineering, University of Michigan, Ann Arbor, Michigan 48109, United States

Hongchao Xie - Department of Physics, University of Michigan, Ann Arbor, Michigan 48109, United States; orcid.org/0000-0001-8525-9852

Nikhil Uday Dhale - Department of Physics, The University of Texas at Dallas, Richardson, Texas 75080, United States

Suk Hyun Sung - Department of Material Science and Engineering, University of Michigan, Ann Arbor, Michigan 48109, United States

Aswin Lakshmi Narayanan Kondusamy – Department of Physics, The University of Texas at Dallas, Richardson, Texas 75080, United States

Xiqu Wang - Department of Chemistry, University of Houston, Houston, Texas 77004, United States

Haonan Zhao – Department of Physics, University of Michigan, Ann Arbor, Michigan 48109, United States

Diana Berman - Department of Materials Science and Engineering, University of North Texas, Denton, Texas 76203, United States; orcid.org/0000-0002-9320-9772

Complete contact information is available at: https://pubs.acs.org/10.1021/acsnano.2c02896

#### **Author Contributions**

W. L. and X. G. contributed equally.

The authors declare no competing financial interest.

# **ACKNOWLEDGMENTS**

We thank Prof. S. Forrest for offering us to use the atomic force microscope in his laboratory to calibrate layer numbers of exfoliated CrSBr. Work conducted at University of Texas at Dallas was supported by the U.S. Air Force Office of Scientific Research grant no. FA9550-19-1-0037. This project is also partially supported by NSF-DMREF-1921581 (magnetic characterizations). L.Z. acknowledges support by NSF CAREER grant no. DMR-174774, AFOSR YIP grant no.

FA9550-21-1-0065, and Alfred P. Sloan Foundation. R.H. acknowledges support from ARO grant no. W911NF-22-1-0056 and the W. M. Keck Foundation. Support from the Advanced Materials and Manufacturing Processes Institute at the University of North Texas is acknowledged.

### **REFERENCES**

- (1) Gong, C.; Li, L.; Li, Z.; Ji, H.; Stern, A.; Xia, Y.; Cao, T.; Bao, W.; Wang, C.; Wang, Y.; Qiu, Z. Q.; Cava, R. J.; Louie, S. G.; Xia, J.; Zhang, X. Discovery of Intrinsic Ferromagnetism in Two-Dimensional van Der Waals Crystals. *Nature* 2017, 546, 265–269.
- (2) Huang, B.; Clark, G.; Navarro-Moratalla, E.; Klein, D. R.; Cheng, R.; Seyler, K. L.; Zhong, Di.; Schmidgall, E.; McGuire, M. A.; Cobden, D. H.; Yao, W.; Xiao, D.; Jarillo-Herrero, P.; Xu, X. Layer-Dependent Ferromagnetism in a van Der Waals Crystal down to the Monolayer Limit. *Nature* **2017**, *546*, 270–273.
- (3) Seyler, K. L.; Zhong, D.; Klein, D. R.; Gao, S.; Zhang, X.; Huang, B.; Navarro-Moratalla, E.; Yang, L.; Cobden, D. H.; McGuire, M. A.; Yao, W.; Xiao, D.; Jarillo-Herrero, P.; Xu, X. Ligand-Field Helical Luminescence in a 2D Ferromagnetic Insulator. *Nat. Phys.* **2018**, *14*, 277–281.
- (4) Chen, B.; Yang, J. H.; Wang, H. D.; Imai, M.; Ohta, H.; Michioka, C.; Yoshimura, K.; Fang, M. H. Magnetic Properties of Layered Itinerant Electron Ferromagnet Fe<sub>3</sub>GeTe<sub>2</sub>. *J. Phys. Soc. Jpn.* **2013**, *82*, 124711.
- (5) May, A. F.; Calder, S.; Cantoni, C.; Cao, H.; McGuire, M. A. Magnetic Structure and Phase Stability of the van Der Waals Bonded Ferromagnet Fe<sub>3-x</sub>GeTe<sub>2</sub>. *Phys. Rev. B* **2016**, *93*, 014411.
- (6) Deng, Y.; Yu, Y.; Song, Y.; Zhang, J.; Wang, N. Z.; Sun, Z.; Yi, Y.; Wu, Y. Z.; Wu, S.; Zhu, J.; Wang, J.; Chen, X. H.; Zhang, Y. Gate-Tunable Room-Temperature Ferromagnetism in Two-Dimensional Fe<sub>3</sub>GeTe<sub>2</sub>. *Nature* **2018**, *563*, 94–99.
- (7) Carteaux, V.; Brunet, D.; Ouvrard, G.; Andre, G. Crystallographic, Magnetic and Electronic Structures of a New Layered Ferromagnetic Compound Cr<sub>2</sub>Ge<sub>2</sub>Te<sub>6</sub>. *J. Phys.: Condens. Matter* **1995**, 7, 69–87.
- (8) Zhuo, W.; Lei, B.; Wu, S.; Yu, F.; Zhu, C.; Cui, J.; Sun, Z.; Ma, D.; Shi, M.; Wang, H.; Wang, W.; Wu, T.; Ying, J.; Wu, S.; Wang, Z.; Chen, X. Manipulating Ferromagnetism in Few-Layered Cr<sub>2</sub>Ge<sub>2</sub>Te<sub>6</sub>. *Adv. Mater.* **2021**, 33, 2008586.
- (9) Hansen, W. N.; Griffel, M. Heat Capacities of CrF<sub>3</sub> and CrCl<sub>3</sub> from 15 to 300 K. *J. Chem. Phys.* **1958**, 28, 902–907.
- (10) Elliott, N.; Hastings, J. Neutron Diffraction Investigation of KCN. *Acta Crystallogr.* **1961**, *14*, 1018–1018.
- (11) Tsubokawa, I. On the Magnetic Properties of a CrBr<sub>3</sub> Single Crystal. *J. Phys. Soc. Jpn.* **1960**, *15*, 1664–1668.
- (12) Dillon, J. F.; Olson, C. E. Magnetization, Resonance, and Optical Properties of the Ferromagnet CrI<sub>3</sub>. *J. Appl. Phys.* **1965**, *36*, 1259–1260.
- (13) McGuire, M. A.; Dixit, H.; Cooper, V. R.; Sales, B. C. Coupling of Crystal Structure and Magnetism in the Layered, Ferromagnetic Insulator CrI<sub>3</sub>. *Chem. Mater.* **2015**, *27*, 612–620.
- (14) Cai, X.; Song, T.; Wilson, N. P.; Clark, G.; He, M.; Zhang, X.; Taniguchi, T.; Watanabe, K.; Yao, W.; Xiao, D.; McGuire, M. A.; Cobden, D. H.; Xu, X. Atomically Thin CrCl<sub>3</sub>: An In-Plane Layered Antiferromagnetic Insulator. *Nano Lett.* **2019**, *19*, 3993–3998.
- (15) Huang, B.; Clark, G.; Klein, D. R.; MacNeill, D.; Navarro-Moratalla, E.; Seyler, K. L.; Wilson, N.; McGuire, M. A.; Cobden, D. H.; Xiao, D.; Yao, W.; Jarillo-Herrero, P.; Xu, X. Electrical Control of 2D Magnetism in Bilayer CrI<sub>3</sub>. *Nat. Nanotechnol.* **2018**, *13*, 544–548.
- (16) Lado, J. L.; Fernández-Rossier, J. On the Origin of Magnetic Anisotropy in Two dimensional CrI<sub>3</sub>. 2D Mater. **2017**, 4, 035002.
- (17) Kim, H. H.; Yang, B.; Li, S.; Jiang, S.; Jin, C.; Tao, Z.; Nichols, G.; Sfigakis, F.; Zhong, S.; Li, C.; Tian, S.; Cory, D. G.; Miao, G. X.; Shan, J.; Mak, K. F.; Lei, H.; Sun, K.; Zhao, L.; Tsen, A. W. Evolution of Interlayer and Intralayer Magnetism in Three Atomically Thin Chromium Trihalides. *Proc. Natl. Acad. Sci. U. S. A.* **2019**, *116*, 11131.

- (18) Tartaglia, T. A.; Tang, J. N.; Lado, J. L.; Bahrami, F.; Abramchuk, M.; McCandless, G. T.; Doyle, M. C.; Burch, K. S.; Ran, Y.; Chan, J. Y.; Tafti, F. Accessing New Magnetic Regimes by Tuning the Ligand Spin-Orbit Coupling in van Der Waals Magnets. *Sci. Adv.* **2020**, *6*, No. eabb9379.
- (19) Abramchuk, M.; Jaszewski, S.; Metz, K. R.; Osterhoudt, G. B.; Wang, Y.; Burch, K. S.; Tafti, F. Controlling Magnetic and Optical Properties of the van Der Waals Crystal CrCl<sub>3-x</sub>Br<sub>x</sub> *via* Mixed Halide Chemistry. *Adv. Mater.* **2018**, *30*, 1801325.
- (20) Tang, C.; Zhang, Z.; Lai, S.; Tan, Q.; Gao, W. bo. Magnetic Proximity Effect in Graphene/CrBr3 van Der Waals Heterostructures. *Adv. Mater.* **2020**, *32*, 1908498.
- (21) Mogi, M.; Nakajima, T.; Ukleev, V.; Tsukazaki, A.; Yoshimi, R.; Kawamura, M.; Takahashi, K. S.; Hanashima, T.; Kakurai, K.; Arima, T. H.; Kawasaki, M.; Tokura, Y. Large Anomalous Hall Effect in Topological Insulators with Proximitized Ferromagnetic Insulators. *Phys. Rev. Lett.* **2019**, *123*, 016804.
- (22) Albarakati, S.; Tan, C.; Chen, Z.; Partridge, J. G.; Zheng, G.; Farrar, L.; Mayes, E. L. H.; Field, M. R.; Lee, C.; Wang, Y.; Xiong, Y.; Tian, M.; Xiang, F.; Hamilton, A. R.; Tretiakov, O. A.; Culcer, D.; Zhao, Y.; Wang, L. Antisymmetric Magnetoresistance in van Der Waals Fe<sub>3</sub>GeTe<sub>2</sub>/Graphite/Fe<sub>3</sub>GeTe<sub>2</sub> Trilayer Heterostructures. *Sci. Adv.* **2019**, *5*, No. eaaw0409.
- (23) Hu, G.; Zhu, Y.; Xiang, J.; Yang, T. Y.; Huang, M.; Wang, Z.; Wang, Z.; Liu, P.; Zhang, Y.; Feng, C.; Hou, D.; Zhu, W.; Gu, M.; Hsu, C. H.; Chuang, F. C.; Lu, Y.; Xiang, B.; Chueh, Y. L. Antisymmetric Magnetoresistance in a van Der Waals Antiferromagnetic/Ferromagnetic Layered MnPS<sub>3</sub>/Fe<sub>3</sub>GeTe<sub>2</sub>Stacking Heterostructure. *ACS Nano* **2020**, *14*, 12037–12044.
- (24) Xie, H.; Luo, X.; Ye, G.; Ye, Z.; Ge, H.; Sung, S. H.; Rennich, E.; Yan, S.; Fu, Y.; Tian, S.; Lei, H.; Hovden, R.; Sun, K.; He, R.; Zhao, L. Twist Engineering of the Two-Dimensional Magnetism in Double Bilayer Chromium Triiodide Homostructures. *Nat. Phys.* **2022**, *18*, 30–36.
- (25) Xu, Y.; Ray, A.; Shao, Y. T.; Jiang, S.; Lee, K.; Weber, D.; Goldberger, J. E.; Watanabe, K.; Taniguchi, T.; Muller, D. A.; Mak, K. F.; Shan, J. Coexisting Ferromagnetic-Antiferromagnetic State in Twisted Bilayer CrI<sub>3</sub>. *Nat. Nanotechnol.* **2022**, *17*, 143–147.
- (26) Song, T.; Sun, Q. C.; Anderson, E.; Wang, C.; Qian, J.; Taniguchi, T.; Watanabe, K.; McGuire, M. A.; Stöhr, R.; Xiao, D.; Cao, T.; Wrachtrup, J.; Xu, X. Direct Visualization of Magnetic Domains and Moiré Magnetism in Twisted 2D Magnets. *Science*. **2021**, *374*, 1140–1144.
- (27) Telford, E. J.; Dismukes, A. H.; Lee, K.; Cheng, M.; Wieteska, A.; Bartholomew, A. K.; Chen, Y. S.; Xu, X.; Pasupathy, A. N.; Zhu, X.; Dean, C. R.; Roy, X. Layered Antiferromagnetism Induces Large Negative Magnetoresistance in the van Der Waals Semiconductor CrSBr. *Adv. Mater.* **2020**, *32*, 2003240.
- (28) Göser, O.; Paul, W.; Kahle, H. G. Magnetic Properties of CrSBr. J. Magn. Magn. Mater. 1990, 92, 129-136.
- (29) Lee, K.; Dismukes, A. H.; Telford, E. J.; Wiscons, R. A.; Wang, J.; Xu, X.; Nuckolls, C.; Dean, C. R.; Roy, X.; Zhu, X. Magnetic Order and Symmetry in the 2D Semiconductor CrSBr. *Nano Lett.* **2021**, *21*, 3511–3517.
- (30) Ghiasi, T. S.; Kaverzin, A. A.; Dismukes, A. H.; de Wal, D. K.; Roy, X.; van Wees, B. J. Electrical and Thermal Generation of Spin Currents by Magnetic Bilayer Graphene. *Nat. Nanotechnol.* **2021**, *16*, 788–794.
- (31) Mangelsen, S.; Bensch, W. HfTe<sub>2</sub>: Enhancing Magnetoresistance Properties by Improvement of the Crystal Growth Method. *Inorg. Chem.* **2020**, *59*, 1117–1124.
- (32) Edelberg, D.; Rhodes, D.; Kerelsky, A.; Kim, B.; Wang, J.; Zangiabadi, A.; Kim, C.; Abhinandan, A.; Ardelean, J.; Scully, M.; et al. Approaching the Intrinsic Limit in Transition Metal Diselenides *via* Point Defect Control. *Nano Lett.* **2019**, *19*, 4371–4379.
- (33) Sung, S. H.; Schnitzer, N.; Brown, L.; Park, J.; Hovden, R. Stacking, Strain, and Twist in 2D Materials Quantified by 3D Electron Diffraction. *Phys. Rev. Mater.* **2019**, *3*, 064003.

- (34) May, A. F.; Liu, Y.; Calder, S.; Parker, D. S.; Pandey, T.; Cakmak, E.; Cao, H.; Yan, J.; McGuire, M. A. Magnetic Order and Interactions in Ferrimagnetic Mn<sub>3</sub>Si<sub>2</sub>Te<sub>6</sub>. *Phys. Rev. B* **2017**, *95*, 174440.
- (35) Angelkort, J.; Wölfel, A.; Schönleber, A.; Van Smaalen, S.; Kremer, R. K. Observation of Strong Magnetoelastic Coupling in a First-Order Phase Transition of CrOCl. *Phys. Rev. B* **2009**, *80*, 144416.
- (36) Zhang, T.; Wang, Y.; Li, H.; Zhong, F.; Shi, J.; Wu, M.; Sun, Z.; Shen, W.; Wei, B.; Hu, W.; Liu, X.; Huang, L.; Hu, C.; Wang, Z.; Jiang, C.; Yang, S.; Zhang, Q. M.; Qu, Z. Magnetism and Optical Anisotropy in van Der Waals Antiferromagnetic Insulator CrOCl. ACS Nano 2019, 13, 11353–11362.
- (37) Telford, E. J.; Dismukes, A. H.; Dudley, R. L.; Wiscons, R. A.; Lee, K.; Yu, J.; Shabani, S.; Scheie, A.; Watanabe, K.; Taniguchi, T.; Xiao, D.; Pasupathy, A. N.; Nuckolls, C.; Zhu, X.; Dean, C. R.; Roy, X. Hidden Low-Temperature Magnetic Order Revealed through Magnetotransport in Monolayer CrSBr. arXiv (Mesoscale and Nanoscale Physics), June 15, 2021, 2106.08471, ver. 1. https://arxiv.org/abs/2106.08471 (accessed 2022-09-20).
- (38) Ramirez, A. P.; Hayashi, A.; Cava, R. J.; Siddharthan, R.; Shastry, B. S. Zero-Point Entropy in 'Spin Ice'. *Nature* **1999**, 399, 333–335.
- (39) Zheng, J.; Ran, K.; Li, T.; Wang, J.; Wang, P.; Liu, B.; Liu, Z. X.; Normand, B.; Wen, J.; Yu, W. Gapless Spin Excitations in the Field-Induced Quantum Spin Liquid Phase of  $\alpha$ -RuCl<sub>3</sub>. *Phys. Rev. Lett.* **2017**, *119*, 227208.
- (40) Liu, X.; Taddei, K. M.; Li, S.; Liu, W.; Dhale, N.; Kadado, R.; Berman, D.; Cruz, C. D.; Lv, B. Canted Antiferromagnetism in the Quasi-One-Dimensional Iron Chalcogenide BaFe<sub>2</sub>Se<sub>4</sub>. *Phys. Rev. B* **2020**, *102*, 180403.